





## Extended time scales of carbonaceous chondrite aqueous alteration evidenced by a xenolith in LaPaz Icefield 02239 (CM2)

Martin R. LEE <sup>1\*</sup>, Cameron FLOYD<sup>1</sup>, Pierre-Etienne MARTIN<sup>1</sup>, Xuchao ZHAO <sup>2</sup>, Ian A. FRANCHI <sup>2</sup>, Laura JENKINS<sup>1</sup>, and Sammy GRIFFIN <sup>1</sup>

<sup>1</sup>School of Geographical and Earth Sciences, University of Glasgow, Glasgow G12 8QQ, UK

<sup>2</sup>School of Physical Sciences, Open University, Milton Keynes MK7 6AA, UK

\*Corresponding author.

Martin R. Lee, School of Geographical and Earth Sciences, University of Glasgow, Glasgow G12 8QQ, UK.  
E-mail: [martin.lee@glasgow.ac.uk](mailto:martin.lee@glasgow.ac.uk)

(Received 25 September 2022; revision accepted 10 March 2023)

**Abstract**—LaPaz Icefield (LAP) 02239 is a mildly aqueously altered CM2 carbonaceous chondrite that hosts a xenolith from a primitive chondritic parent body. The xenolith contains chondrules and calcium- and aluminum-rich inclusions (CAIs) in a very fine-grained matrix. The chondrules are comparable in mineralogy and oxygen isotopic composition with those in the CMs, and its CAIs are also mineralogically similar to the CM population apart for being unusually small and abundant. The presence of serpentine demonstrates that the xenolith has been aqueously altered, and its phyllosilicate-rich matrix has a comparable oxygen isotopic composition to the matrices of CM meteorites. The xenolith's chondrules lack fine-grained rims, whereas the xenolith itself has a fine-grained rim that is petrographically and chemically comparable with the rims on coarse grained objects in LAP 02239 and other CM meteorites. These properties show that the xenolith's parent body was formed from similar materials to the CM parent body(ies). Following its lithification by aqueous alteration, a piece of the xenolith's parent body was impact-ejected, acquired a fine-grained rim while free-floating in the protoplanetary disc, then was accreted along with rimmed chondrules and other materials to make the LAP 02239 parent body. Subsequent aqueous processing of the LAP 02239 parent body altered the fine-grained rims on the xenolith, chondrules, and CAIs. The xenolith shows that the timespan of geological evolution of carbonaceous chondrite parent bodies was sufficiently long for some of them to have been aqueously altered before others had formed.

### INTRODUCTION

The Mighei-like (CM) carbonaceous chondrite (CC) meteorites have close spectroscopic affinities to C-complex asteroids (Burbine, 2016) and so likely sample one or more of them. The parent body(ies) of the CMs were formed by the accretion of relatively coarse-grained objects (i.e., chondrules and calcium- and aluminum-rich inclusions [CAIs]) together with fine-grained material that forms the enclosing matrix (Barber, 1981; McSween Jr. & Richardson, 1977). The chondrules and other coarse-grained objects typically have fine-grained rims that they acquired while free-floating in the protoplanetary disc (Hanna &

Ketcham, 2018; Metzler et al., 1992). The constituents of the coarse-grained objects, fine-grained rims and matrix (anhydrous silicates, metal, sulfides, oxides, and amorphous materials) were partially to completely altered by parent body aqueous activity at ~4563 Ma (Bunch & Chang, 1980; Fujiya et al., 2012; McSween Jr., 1979a, 1979b). The resultant secondary minerals are volumetrically dominated by phyllosilicates that are intergrown with carbonates, oxides, and sulfides (Barber, 1981; Bunch & Chang, 1980; Fuchs et al., 1973; Howard et al., 2009, 2011, 2015; Lee et al., 2014; Tomeoka & Buseck, 1985; Trigo-Rodríguez et al., 2019; Zolensky et al., 1993). The CMs are classified by petrologic type/subtype using various properties that

quantitatively or qualitatively describe the degree of aqueous alteration of the accreted anhydrous materials (Alexander et al., 2013; Howard et al., 2015; Rubin et al., 2007; Zolensky et al., 1997). Lithologies that have escaped aqueous alteration and are phyllosilicate free have a petrologic type 3.0/subtype CM3.0, whereas the most highly aqueously altered lithologies that retain none of the original anhydrous constituents have a petrologic type 1.0/subtype CM2.0.

Many of the CMs are breccias, and the most common clasts in these fragmental rocks are CM lithologies, which are termed “cognate clasts” (Bischoff et al., 2006). These clasts can be distinguished from their host meteorite by differences in properties including mineralogy and petrofabric (Figure 1a). The brecciation and mixing of clasts was by impacts in a regolith environment (Bischoff et al., 2006). CM meteorites can also contain fragments of non-CM lithologies (i.e., xenoliths, Table 1), which are typically less than ~5 mm in size. The most abundant types of xenoliths are rich in magnetite relative to the host CM and are similar in mineralogy and texture to C1 meteorites (Zolensky et al., 1997; Figure 1b). Xenoliths have also been described with affinities to other groups of CC meteorites, and in very rare cases to achondrites (Table 1). As they may sample parent bodies that are not represented in meteorite collections, xenoliths can provide a unique window into the composition and evolution of the protoplanetary disc (e.g., Nittler et al., 2019).

Here we describe a chondritic xenolith in the CM2 meteorite LaPaz Icefield (LAP) 02239 that is lithologically distinct from any of the xenoliths that have been described previously (Figure 1c). This xenolith is potentially highly significant because it has a fine-grained rim in common with chondrules, CAIs, and other objects in the CMs (Metzler et al., 1992; Trigo-Rodriguez et al., 2006). As the presence of a rim shows that the xenolith was free-floating in the protoplanetary disc along with chondrules and CAIs before being accreted to make the LAP 02239 parent body, it provides an opportunity to study the composition and geological evolution of an early formed CC body. One aspect that is of particular interest here is whether this

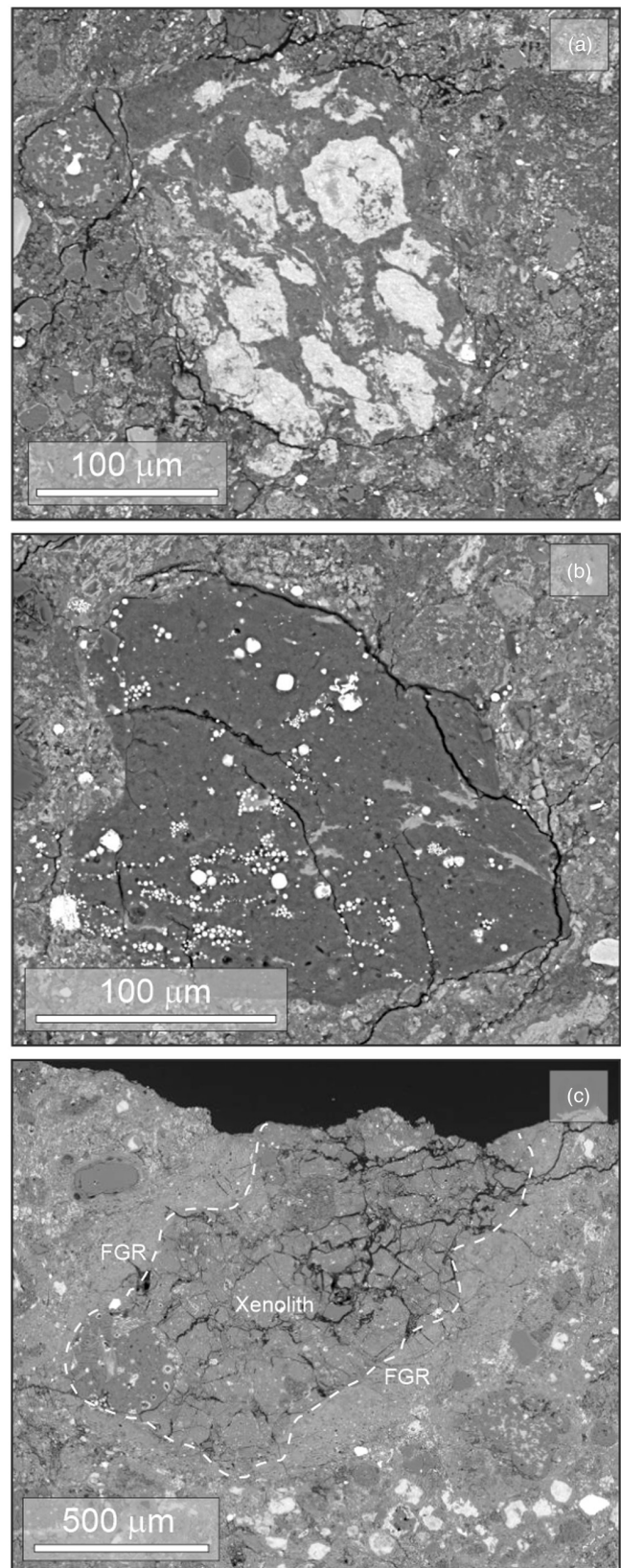


FIGURE 1. (a) Backscattered electron (BSE) image of a cognate clast in Kolang, which stands out from the enclosing meteorite by virtue of its abundant tochilinite–cronstedtite intergrowths (TCIs) (white). Elongation of some of the TCIs is suggestive of a NNW–SSE-oriented petrofabric. (b) BSE image of a C1 xenolith in Cold Bokkeveld that is characterized by abundant cubes and framboids of magnetite (white). Neither the cognate clast (a) nor the xenolith (b) has a fine-grained rim. (c) BSE image of the xenolith that is described in the present study (outlined by a dashed white line). It is enclosed in a fine-grained rim (FGR).

TABLE 1. Xenoliths previously described from CM carbonaceous chondrite meteorites.

Host meteorite	Xenolith's affinity
Aguas Zarcas	Unsampled CC parent body; a petrologic type 1 CC lithology <sup>a</sup>
Cold Bokkeveld	Ureilite meteorites <sup>b</sup>
Grove Mountains (GRO) 021536	CV3 meteorites <sup>c</sup>
Lonewolf Nunataks (LON) 94101	Petrologic type 1, 2, and 3 CCs <sup>d</sup>
Mighei	Petrologic type 3 CCs <sup>b</sup>
Murchison	Petrologic type 3 CC lithologies similar to CO3s and CV3s <sup>e</sup> ; CO3 and CV3 meteorites <sup>f</sup> ; Interior of a CM parent body <sup>g</sup>
Murray	C3 meteorites <sup>h</sup>
Northwest Africa (NWA) 12651	An igneous fragment formed in the CC region <sup>i</sup>

Note: Clasts with a C1 affinity are commonplace in the CMs but rarely recorded (Russell et al., 2022).

<sup>a</sup>Kerraouch et al. (2021).

<sup>b</sup>Muller (1966).

<sup>c</sup>Zhang et al. (2010).

<sup>d</sup>Lindgren et al. (2013).

<sup>e</sup>Fuchs et al. (1973).

<sup>f</sup>Olsen et al. (1988).

<sup>g</sup>Kerraouch et al. (2019).

<sup>h</sup>Bunch and Chang (1980).

<sup>i</sup>Ebert, Patzek, et al. (2019).

primitive body was aqueous altered because such a finding may provide new insights into the distribution and chronology of liquid water in the early solar system.

## MATERIALS AND METHODS

LAP 02239 is a 39.3 g Antarctic find that was recovered in 2002, and is paired with LAP 02333. Both meteorites have a weathering grade of B and a fracturing grade of A/B (Russell et al., 2004). This study used polished block LAP 02239,5 that is rectangular in shape (~9.5 × 8.0 mm) with a surface area of 76.68 mm<sup>2</sup> (Figure 2a,c,d). Clasts and xenoliths were also studied in polished thin sections of the CMs Cold Bokkeveld (BM1727 P19526 loaned by the Natural History Museum, London) and Kolang (made at the University of Glasgow [UoG] from a commercially obtained chip; Figure 1a).

The modal mineralogy of LAP 02333 as quantified by XRD (vol%) is: 51.7% Mg,Fe serpentine, 21.6% cronstedtite, 12.2% olivine, 10.4% pyroxene, 1.8 magnetite, 1.4 sulfide and 0.9% calcite (Howard et al., 2015). The abundance of phyllosilicate relative to anhydrous silicates gives a petrologic type of 1.5 (Howard et al., 2015). From the amount of H in water/OH, Alexander et al. (2013) determined the petrologic types of 1.7 and 1.5 for LAP 02239 and LAP 02333, respectively. A bulk sample of LAP

02239 evolved 8.5 wt% H<sub>2</sub>O with a δD of −43‰ during stepwise pyrolysis, which is comparable with mildly aqueously altered CMs (Lee et al., 2021).

Samples were characterized at the UoG using a Zeiss Sigma field-emission SEM equipped with a silicon-drift energy-dispersive X-ray detector (EDS) operated through Oxford Instruments INCA and AZtec software. Backscattered electron (BSE) images and X-ray maps were obtained at 20 kV/2 nA. Quantitative chemical analyses were acquired at 20 kV/2 nA, with beam currents monitored using a Faraday cup. Spectra were collected for 60 s and quantified via INCA. Calibration used the following mineral standards, with typical detection limits (wt % element) in parentheses: Na, jadeite (0.10); Mg, periclase (0.06); Al, corundum (0.10); Si, diopside (0.11); P, apatite (0.12), S, pyrite (0.10), K, orthoclase feldspar (0.12); Ca, wollastonite (0.10); Ti, rutile (0.16); Cr, chromite (0.19); Mn, rhodonite (0.21); Fe, almandine garnet (0.23); and Ni, Ni metal (0.39).

Oxygen isotope measurements of olivine and pyroxene as well as phyllosilicate-rich areas of matrix were made on the Cameca NanoSIMS 50L at the Open University (OU). Prior to analysis, each area was pre-sputtered with a 100 pA Cs<sup>+</sup> probe for 3 min over an area of 7 × 7 μm to remove C coat and surface contamination, and achieve sputter equilibrium. Analyses were performed with a 100 pA Cs<sup>+</sup> probe rastered over 5 × 5 μm in “spot” mode. An electron flood gun was used for charge compensation. Seven different secondary ion species were collected simultaneously, with <sup>16</sup>O<sup>−</sup> measured on a Faraday detector while <sup>17</sup>O<sup>−</sup>, <sup>18</sup>O<sup>−</sup>, <sup>30</sup>Si<sup>−</sup>, <sup>24</sup>Mg<sup>16</sup>O<sup>−</sup>, <sup>40</sup>Ca<sup>16</sup>O<sup>−</sup>, and <sup>56</sup>Fe<sup>16</sup>O<sup>−</sup> were measured on electron multipliers. A mass resolving power of ~10,000 (Cameca definition; see Hoppe et al., 2013) was used that is sufficient to resolve the <sup>16</sup>OH<sup>−</sup> interference from the <sup>17</sup>O<sup>−</sup> signal.

Analyses lasted approx. 7 min, providing a total of ~1.5 × 10<sup>10</sup> counts <sup>16</sup>O<sup>−</sup>. Analyses were corrected for instrumental mass fractionation against a standard sample of Fo<sub>90</sub> San Carlos olivine (δ<sup>18</sup>O 4.91‰ as measured by laser fluorination at the OU), that was analyzed before and after each block of unknown samples. Analytical uncertainty (all 2σ SD), incorporating internal counting statistics from the sample measurement and external precision from standard replicates analyzed before and/or after the samples, is typically ±1.2‰ for δ<sup>17</sup>O, ±0.8‰ for δ<sup>18</sup>O, and approximately ±1.0‰ for Δ<sup>17</sup>O. Matrix correction was applied to account for differences in the Fe/Mg of the samples of olivine and pyroxene to the standard, and used San Carlos olivine (Fo<sub>90</sub>), Eagle Station pallasite (Fo<sub>80</sub>), and an olivine with a composition of Fo<sub>72</sub>, generating a correction of 0.8‰ offset between the sample and San Carlos olivine.

Analyses of the matrix areas were subjected to much higher <sup>16</sup>OH<sup>−</sup> signal than the olivine and pyroxene



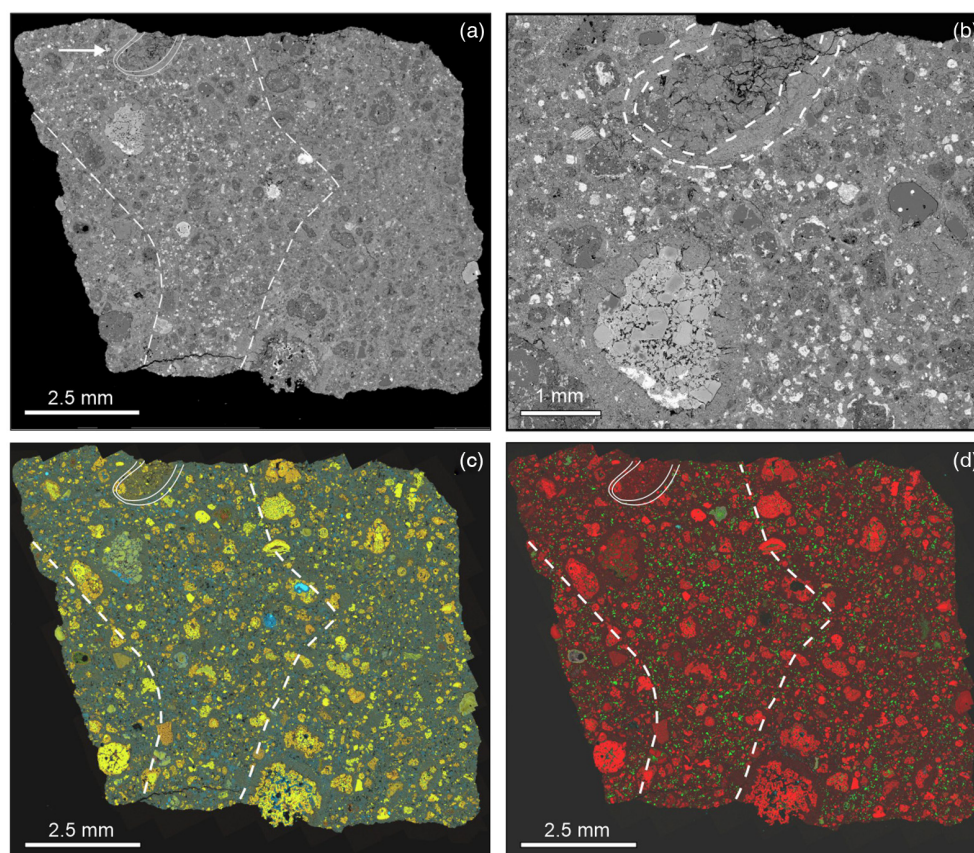


FIGURE 2. Backscattered electron (BSE) images and X-ray maps of LAP 02239. In (a), (c), and (d), the edges of the light lithology are delineated by dashed white lines. (a) BSE image of the whole polished block. The light lithology is defined by the concentration of grains that have a high mean atomic number (white). The xenolith is within the light lithology at the top edge of the block (arrowed). Narrow solid white lines delineate the interface between the xenolith and its fine-grained rim, and between the fine-grained rim and the host meteorite. (b) BSE image showing the xenolith in context. The inner and outer edges of the xenolith's fine-grained rim are delineated by dashed white lines. (c) Color blended X-ray map of the polished block with Fe blue, Mg light green and Si red. These colors render En-rich clinopyroxene orange, Fo-rich olivine yellow, the matrix brown and Fe-metal light blue. (d) Color blended X-ray map of the polished block with Mg red, Ca light green, and Al blue. These colors render clinopyroxene and olivine light red and Ca-carbonate green. (Color figure can be viewed at [wileyonlinelibrary.com](http://wileyonlinelibrary.com).)

standards. In such circumstances, the mass resolving power employed results in a small contribution of  $^{16}\text{OH}^-$  to the  $^{17}\text{O}^-$  signal. To correct for this interference, the  $^{16}\text{OH}^-$  signal was measured for 10 s at the start and end of each measurement, and the  $\delta^{17}\text{O}$  adjusted according to a calibration of  $\Delta^{17}\text{O}$  versus  $^{16}\text{OH}^-/^{16}\text{O}^-$  measured intensity determined by analyses of a terrestrial serpentine versus San Carlos olivine. The  $\delta^{18}\text{O}$  and  $\delta^{17}\text{O}$  of the matrix measurements were corrected against San Carlos olivine, although some variation in matrix composition would be expected. Although not determined in this study, the difference in the matrix effect between San Carlos olivine and a number of serpentines is restricted to a narrow range from  $-1$  to  $+1.6\text{‰}$  (Scicchitano et al., 2018). Therefore, as the matrix potentially contains a number of very fine-grained phases, the use of San Carlos olivine is warranted to

provide a good approximation of the instrumental matrix effect.

The size of whole chondrules was determined from BSE images by image segmentation using GNU Image Manipulation Program and ImageJ software (the Chondrule Image Segmentation method as described by Floyd & Lee, 2022a). Whole chondrules were identified as being polymineralic, rounded over  $>50\%$  of their perimeter, not cut by any large fractures or the edge of the sample, and having less than  $50\%$  internal area removed by polishing. The terminology for CAI morphology and mineralogy follows MacPherson and Davis (1994), and CAIs size was determined using the protocol of Rubin (2007, 2015). Specifically, each CAI was measured along its major axis (c) and the longest dimension at  $90^\circ$  to c (i.e., minor axis). CAI size is

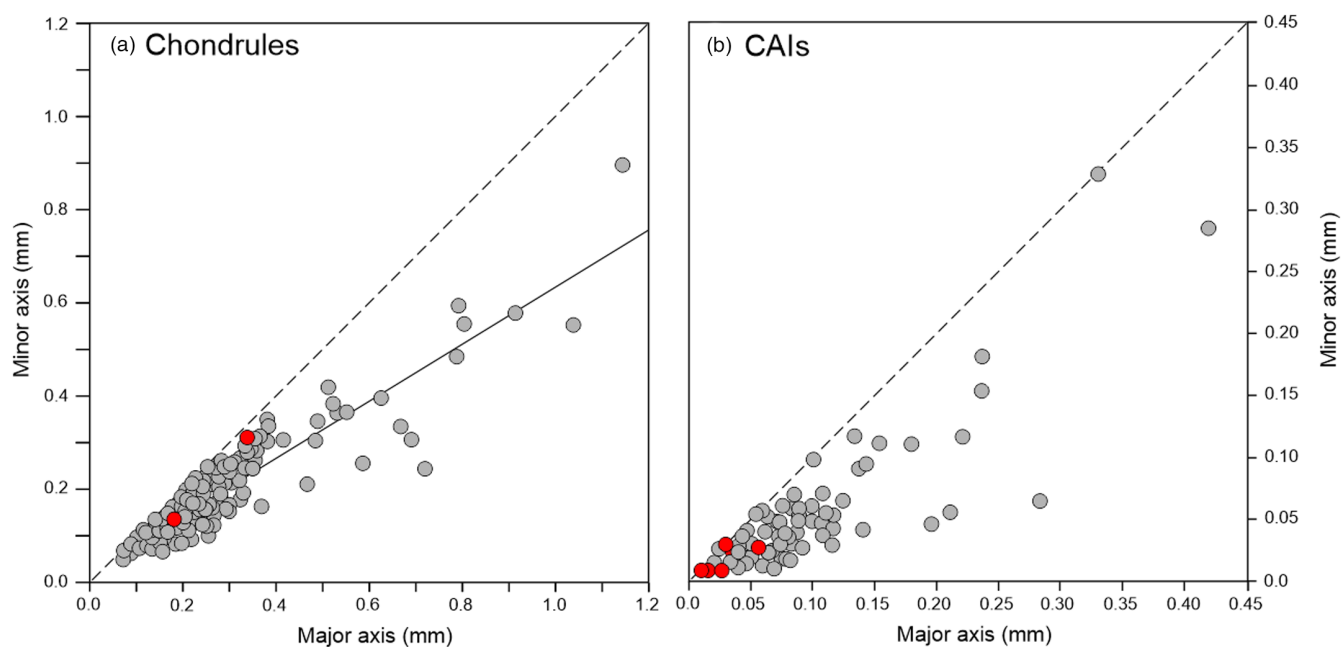


FIGURE 3. Plots of the long axis versus short axis sizes of chondrules and calcium- and aluminum-rich inclusions (CAIs) in both lithologies of LAP 02239 (gray points) and in the xenolith (red points). Those with an aspect ratio of 1 would plot on the dashed 1:1 line. (a) The 150 whole chondrules in LAP 02239 and two in the xenolith. The solid black line is a regression line through the 150 points ( $R^2 = 0.85$ ). (b) The 70 CAIs in LAP 02239 and six in the xenolith. Both whole CAIs and fragments are included in the plot. The data are listed in Tables S1 (chondrules) and S2 (CAIs). (Color figure can be viewed at [wileyonlinelibrary.com](http://wileyonlinelibrary.com).)

expressed as the average of the two measurements, and surface area as the product of the two measurements.

Electron transparent wafers for transmission electron microscopy (TEM) were cut and extracted from the xenolith's matrix using a FEI DualBeam focused ion beam (FIB) instrument in the School of Physics and Astronomy, UoG. The instrument was operated at 30 kV, with different beam currents used during the milling process. Wafers were extracted using an in situ micromanipulator and welded to the tines of a copper holder using electron and ion beam deposited platinum (Lee et al., 2003). The wafers were characterized by bright-field TEM imaging and selected area electron diffraction (SAED) using a FEI T20 TEM operated at 200 kV.

## RESULTS

### Petrography, Mineralogy, and Mineral Chemistry of the LAP 02239 Meteorite

LAP 02239 contains two main lithologies, hereafter referred to as “dark” and “light” from their overall appearance in BSE images (Figure 2a). Both lithologies contain chondrules, chondrule fragments, CAIs, and coarse anhydrous mineral grains, and most of those objects have a fine-grained rim. Between the rimmed objects is a fine-grained matrix. The xenolith is in the light lithology (Figure 2b), and neither lithology has any other clasts.

The polished block is 75.53 mm<sup>2</sup> in size excluding the xenolith, and 24.58% of that area comprises whole chondrules and chondrule fragments. There are 150 whole chondrules (2.0 whole chondrules/mm<sup>2</sup>), 144 type I and six type II (Figure 2a,c,d), all with a fine-grained rim, and they occupy 11.4% of the area of the polished block. The whole chondrules range in major axis/minor axis size from 1.145/0.900 mm (−0.195/0.152  $\phi$ ) to 0.072/0.051 mm (3.796/4.293  $\phi$ ; Figure 3a). Their average major axis size is 0.224 mm (2.157  $\phi$ ), and the average minor axis size is 0.164 mm (2.603  $\phi$ ; Table S1). All of the whole chondrules have an aspect ratio of greater than 1 (average of 1.44), and their long axes define a weak compactional petrofabric (Figure S1). Chondrule olivine and pyroxene grains are typically pristine and can host blebs of Fe,Ni metal. The mesostasis glass of all chondrules has been aqueously altered to phyllosilicate or removed by dissolution to leave voids.

There are 70 CAIs in the polished block (excluding the xenolith). Their major axis versus minor axis sizes are plotted in Figure 3b and listed in Table S2. Their size and abundance are also summarized in Table 2. Sixty percent are simple inclusions, 30% are simple aggregates, and 10% are complex aggregates. The mineralogy of each CAI is in Table S2, and of note is that 24% contain hibonite and 36% phyllosilicate. Of the 70 CAIs, 62 have a fine-grained rim. There is some correlation between the presence of a fine-grained rim and size in that 5 of the 10 smallest CAIs (all less than 30  $\mu$ m in size) are un-rimmed (Table S2).

TABLE 2. Abundance and size of calcium- and aluminum-rich inclusions (CAIs) in LAP 02239, its xenolith, and four other CMs from the literature.

	Number of CAIs/sample area <sup>a</sup>	CAIs/mm <sup>2</sup>	Size range, average <sup>b</sup>	Proportion of sample area that is CAIs (%)
LAP 02239	70/75.53 mm <sup>2</sup>	0.93	14–352 $\mu\text{m}$ , $72 \pm 59 \mu\text{m}$	0.72
LAP 02239 xenolith <sup>c</sup>	6/0.824 mm <sup>2</sup>	7.28	10–48 $\mu\text{m}$ , $26 \pm 14 \mu\text{m}$	0.56
QUE 97990 <sup>d</sup>	32/50 mm <sup>2</sup>	0.64	33–525 $\mu\text{m}$ , $122 \pm 97 \mu\text{m}$	1.43
Paris <sup>d</sup>	18/108 mm <sup>2</sup>	0.17	33–172 $\mu\text{m}$ , $111 \pm 39 \mu\text{m}$	0.21
Mighei <sup>e</sup>	35/not stated	~0.10	25–1150 $\mu\text{m}$ , $181 \pm 206 \mu\text{m}$	n.a.
NWA 11024 <sup>f</sup>	82/~135 mm <sup>2</sup>	0.61	~15–490 $\mu\text{m}$ , n.a.	1.3

Abbreviation: n.a., not applicable.

<sup>a</sup>Both intact and fragments.

<sup>b</sup> $\pm$  is the standard deviation.

<sup>c</sup>The area of the xenolith excludes its fine-grained rim.

<sup>d</sup>Data for Queen Alexandra Range (QUE) 97990 and Paris are from Rubin (2007) and Rubin (2015), respectively, and to facilitate comparison with the present study pyroxene inclusions and pyroxene–olivine inclusions are not included.

<sup>e</sup>Data from MacPherson and Davis (1994), who estimate that the meteorite has ~10 CAIs/cm<sup>2</sup>.

<sup>f</sup>Data from Ebert, Bischoff, et al. (2019) and are from two thin sections (~80 and ~55 mm<sup>2</sup>) with CAI abundances of 1.4 and 1.1 vol%.

The fine-grained rims on chondrules, chondrule fragments, and CAIs are similar in petrographic appearance (Figure 4a). They contain ~2–10  $\mu\text{m}$  diameter pores, which are most common in their outer parts, and the similarities in size and shape of these pores between rims in different areas of the sample argue against them being a polishing artifact. Most rims also have fractures that are oriented approximately normal to their inner and outer edges, and are inferred to be original features (Figure 4b). The rims have a Mg-Fe silicate composition (Table 3). In a (Si + Al)-Mg-Fe ternary diagram, individual analyses plot on or just below the serpentine solid solution line and are compositionally comparable with fine-grained rims in other CM chondrites (Figure 5a).

In addition to chondrules, chondrule fragments, and CAIs, LAP 02239 contains grains that are a few tens of micrometers in size and have a high mean atomic number (Z) making them bright in BSE images (Figure 6a,b). It is the concentration of these grains in one part of the polished block that defines the light lithology; in all other respects, the two lithologies are indistinguishable (Figure 2a). The grains are roughly equant in shape, sometimes with faceted edges, and are composed of arrays of closely packed ~10  $\mu\text{m}$  long fibers. The fibers radiate inwards from the outer edges of the grains and may also radiate outwards from points close to their center (Figure 6a). Many of these grains contain crystals of Ca-carbonate (aragonite/calcite) that are ~20 to 30  $\mu\text{m}$  in size and are inclusion free (Figure 6b). Edges of the Ca-carbonate crystals may be sharp or embayed by arrays of fibers. The grains are rich in O, Mg, Si, S, Fe, and Ni; as these compositions do not match that of any one mineral, the grains are interpreted to be composed of an intergrowth of two or more phases. Plotted on a (Si + Al)-S-(Mg + Fe) ternary diagram analyses lie approximately on a line

between tochilinite and serpentine (Figure S2), and so are hereafter referred to as “tochilinite–serpentine grains” (Table 3). Given the high Z of these grains, the serpentine will be Fe rich. The tochilinite–serpentine grains have ~10 to 15  $\mu\text{m}$ -wide rims that thicken and thin over depressions and protuberances, respectively, to give the rimmed grains a rounded profile (Figure 6a). The rims are very similar in petrographic appearance and chemical composition to the fine-grained rims on chondrules and CAIs elsewhere in LAP 02239 (Table 3; Figure 5c), although that does not necessarily mean that they are formed in the same way.

The matrix of LAP 02239 contains sulfide grains ~80–90  $\mu\text{m}$  in size that are made of pyrrhotite with a ~2–4  $\mu\text{m}$  rim of pentlandite. Within the pyrrhotite are ~10  $\mu\text{m}$  size patches of magnetite that are typically associated with fractures (Figure 6c). These sulfides closely resemble the “pyrrhotite–pentlandite intergrowth altered to magnetite” (PPI alt) grains that have been described from other CMs by Singerling and Brearley (2020). Two large grains of Fe,Ni metal occur in the light lithology, one of which is within a type I chondrule (Figure 6d). In both cases, the metal has been extensively altered to a Fe-oxide with detectable Cl and S (in EDS spectra) that is interpreted to be akaganéite (Buchwald & Clarke, 1995).

### Petrography and Mineralogy of the Xenolith

The xenolith is roughly oval in shape, although part of it has been lost at the edge of the polished block (Figure 2b). It is 1.26/0.65 mm in major axis/minor axis size and has a surface area of 0.824 mm<sup>2</sup>. The xenolith has a fine-grained rim that is ~50 to 150  $\mu\text{m}$  thick and with a surface area of 0.327 mm<sup>2</sup> (Figures 2b and 7a,b). Within the xenolith are chondrules, chondrule fragments, and CAIs that are



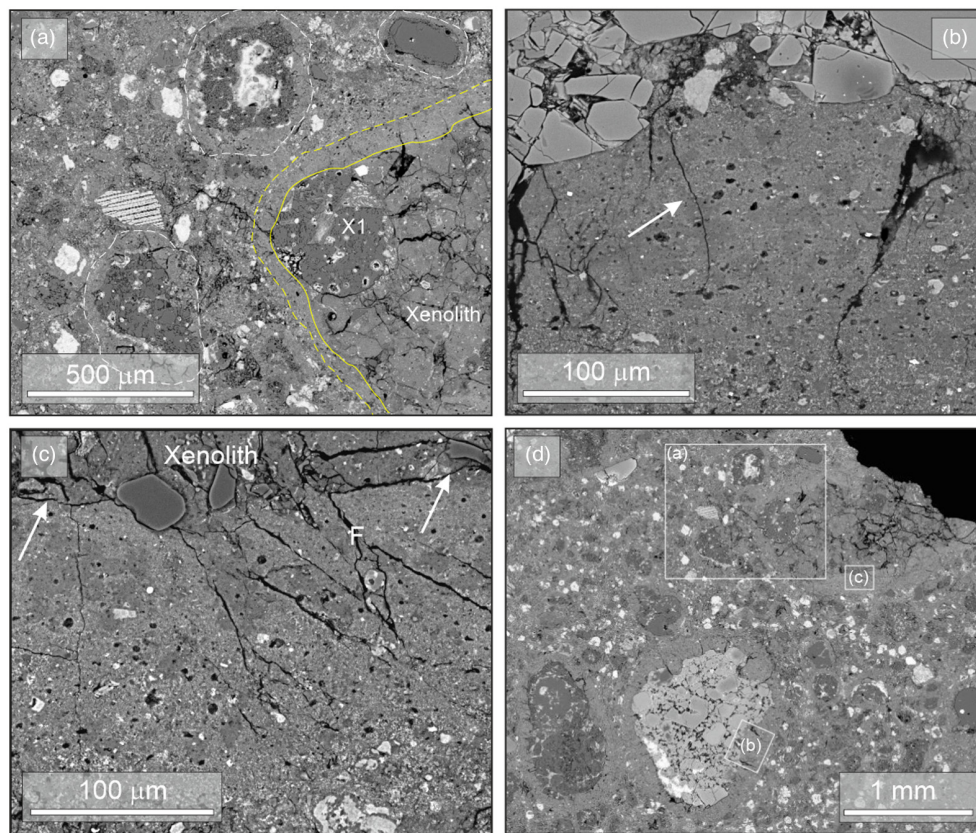


FIGURE 4. Backscattered electron (BSE) images of fine-grained rims in the LAP 02239 polished block. (a) Part of the xenolith (right hand side) and the host meteorite. The outer edge of the xenolith is delineated by a solid yellow line, and the outer edge of its fine-grained rim by a dashed yellow line. The outer edges of fine-grained rims on two chondrules and on a mineral grain in the host meteorite are delineated by dashed white lines. Note that a whole chondrule in the xenolith (X1) lacks a fine-grained rim despite being similar in size to the three rimmed objects in the host meteorite. (b) The fine-grained rim on a type II chondrule in the light lithology (the chondrule is at the top of the image). The rim contains small pores (black) and is cut by narrow fractures, one of which is indicated by a white arrow. (c) The xenolith's fine-grained rim. The xenolith is at the top edge of the image and labeled. Note the sharp contact between the xenolith's matrix and its fine-grained rim (arrowed). Some fractures (F) can be traced from the matrix into the fine-grained rim. (d) Locations of images in (a), (b), and (c) in the LAP 02239 polished block. (Color figure can be viewed at [wileyonlinelibrary.com](http://wileyonlinelibrary.com).)

supported in a very fine-grained matrix. None of these objects has a fine-grained rim (Figures 4a and 7c,d).

The xenolith contains two whole chondrules (X1 and X2, both type I POP) and four fragments of type I chondrules (i.e., 2.4 whole chondrules/mm<sup>2</sup>; Figures 4a and 7a–c). They have a major axis/minor axis size of 0.339/0.310 mm (X1) and 0.180/0.137 mm (X2) (Figure 3a) and together occupy a surface area of 0.10 mm<sup>2</sup> corresponding to 12.4% of the area of the xenolith (Table S1). X1, the largest of the two whole chondrules, contains phenocrysts of forsterite (Fo<sub>98.7</sub>) and enstatite (En<sub>98.0</sub>Fs<sub>1.2</sub>Wo<sub>0.8</sub>), and its mesostasis has a Mg-Fe silicate composition (Table 3). This chondrule also hosts several ~20–30 μm diameter voids that are circular to oval in shape and have a Fe-rich lining (Figure 7c). Oxygen isotope analyses of olivine and pyroxene grains in the two chondrules are listed in Table 4. Taken together, they range in δ<sup>18</sup>O and δ<sup>17</sup>O values from –3.5‰ to

+0.5‰ and –7.1‰ to –3.3‰, respectively. All analyses plot within the error of the carbonaceous chondrite anhydrous mineral (CCAM) line (Figure 8). The xenolith has six CAIs, giving an abundance of 7.28/mm<sup>2</sup>, and they are small (26 μm average size) relative to CAIs in the host meteorite (Table 2). All six are simple inclusions with three containing phyllosilicate and one with hibonite (Figure 7d; Table S2).

The xenolith's matrix contains ~15–40 μm size angular grains (mostly olivine), a smaller number of larger olivine grains that can contain beads of Fe,Ni metal, and two sulfide grains. One of the sulfides is a 20 μm grain of pyrrhotite associated with a small lath of Fe,Ni phosphide (probably schreibersite), and the other is a 25 μm crystal of pyrrhotite that has a 4 μm-wide rim of pentlandite (Figure 7e); the latter is comparable with the “pyrrhotite–pentlandite intergrowth” (PPI) grains that have been described from the CMs (Singerling & Brearley, 2018). The

TABLE 3. Chemical composition of constituents of LAP 02239 and the xenolith (wt%).

	LAP 02239						Xenolith					
	Tochilinite– serpentine grains		Tochilinite– serpentine grains' rim		Chondrule FGRs		Xenolith's FGR		Matrix		Chondrule X1 mesostasis	
	wt%	±	wt%	±	wt%	±	wt%	±	wt%	±	wt%	±
SiO <sub>2</sub>	11.31	1.14	22.28	1.69	22.85	2.21	22.95	1.18	28.17	0.89	26.84	4.70
TiO <sub>2</sub>	n.a.		d.l.		n.a.		n.a.		n.a.		0.10	0.18
Al <sub>2</sub> O <sub>3</sub>	1.94	0.26	2.52	0.29	2.97	0.59	2.99	0.50	1.96	0.15	4.31	1.28
Cr <sub>2</sub> O <sub>3</sub>	d.l.		0.14	0.17	0.30	0.15	0.23	0.19	0.52	0.10	0.52	0.04
FeO	49.15	2.82	27.39	2.25	26.55	2.16	27.22	1.70	19.58	0.89	29.46	3.39
MnO	0.02	0.08	d.l.		0.04	0.10	0.04	0.10	0.08	0.13	0.13	0.23
MgO	7.59	0.80	11.42	1.95	12.18	1.22	12.46	0.78	17.58	0.67	11.81	1.09
CaO	0.02	0.07	0.36	0.13	0.46	0.48	0.74	0.35	0.26	0.10	2.76	2.02
Na <sub>2</sub> O	0.20	0.14	0.35	0.06	0.57	0.17	0.38	0.20	0.53	0.09	0.27	0.04
P <sub>2</sub> O <sub>5</sub>	d.l.		0.10	0.15	0.23	0.25	0.39	0.28	0.05	0.12	d.l.	
NiO	3.51	0.73	1.72	0.51	1.91	0.28	1.84	0.20	2.42	0.26	0.23	0.39
S	10.89	0.89	2.40	0.44	2.60	0.29	2.61	0.19	2.79	0.20	0.67	0.44
Total	84.64	2.48	72.75	2.80	70.66	4.20	71.84	2.02	74.94	1.55	77.09	6.34
<i>n</i>	24		9		22		16		18		3	

Note: All of the analyses are listed in Table S3.

Abbreviations: FGR, fine-grained rims; d.l., below the limits of detection; n.a., not analyzed; ±, the standard deviation.

matrix also contains high-Z patches ~10 µm in size that have a central void and sometimes also contain small grains of Fe-sulfide. TEM images and SAED patterns of the xenolith's matrix reveal lath-shaped crystals that are a few hundred nanometers in length and with a 0.72 nm basal layer spacing that is diagnostic of serpentine (Figure 7f). The xenolith's matrix is heavily fractured; the fractures do not cut the two whole chondrules, although some extend part way into the xenolith's fine-grained rim (Figure 7c). Chemical analyses of the xenolith's matrix plot just above the serpentine solid solution line, and at the Fe-poor end of a trend defined by the matrices of CM chondrites (Figure 5d). Seven NanoSIMS analyses were obtained from the matrix. They range in δ<sup>18</sup>O and δ<sup>17</sup>O from 8.5‰ to 12.7‰, and 2.8‰ to 5.6‰, respectively, and all plot below the CCAM line (Figure 8). While some of this range in δ<sup>18</sup>O may be the result of matrix effects associated with variability in the composition of the target areas, which have not been corrected for, it should be noted that the variability in measured ion beam intensities of Si/O and MgO/O reveals variations of 10%–15%. Thus, there was limited variation in average composition, and therefore matrix effects would not be expected to exceed 1–2‰. Reported Δ<sup>17</sup>O values would not be affected by any matrix effects.

The xenolith's fine-grained rim is petrographically comparable with rims on other objects in LAP 02239 including having small (~4–10 µm) pores that are most abundant in its outer part (Figure 4c). This rim is also close in chemical composition to fine-grained rims elsewhere in LAP 02239 and other CMs (Table 3; Figure 5b).

## DISCUSSION

We first evaluate the affinity of LAP 02239 and its xenolith relative to CC meteorite groups, then outline the xenolith's history from accretion of its own parent body to lithification of the LAP 02239 parent body. Finally, we consider why rimmed xenoliths are so scarce, and the insights they can provide into the accretion and geological evolution of CC parent bodies.

### Classification and Alteration of the LAP 02239 Meteorite

The light and dark lithologies of LAP 02239 are petrographically consistent with a CM as they contain rimmed chondrules, chondrule fragments, and CAIs in a fine-grained matrix. The mineralogy and chemical composition of both lithologies indicate that they have been mildly aqueously altered. For example, the olivine and pyroxene phenocrysts of chondrules are unaltered, and can contain beads of Fe,Ni metal; yet, the mesostasis of chondrules has been replaced by phyllosilicates or lost by dissolution. Also, Ca-carbonate is abundant, whereas dolomite is absent. These properties indicate that LAP 02239 has a petrologic subtype of ~CM2.4–2.5 (Rubin et al., 2007), which is consistent with petrologic types of 1.5 and 1.5–1.7 that were determined for bulk samples of LAP 02239 and its pair (Alexander et al., 2013; Howard et al., 2015).

Another property that can be used to help constrain the petrologic subtype of a CM is the chemical composition of its grains of “poorly characterized phases” (PCP; Rubin



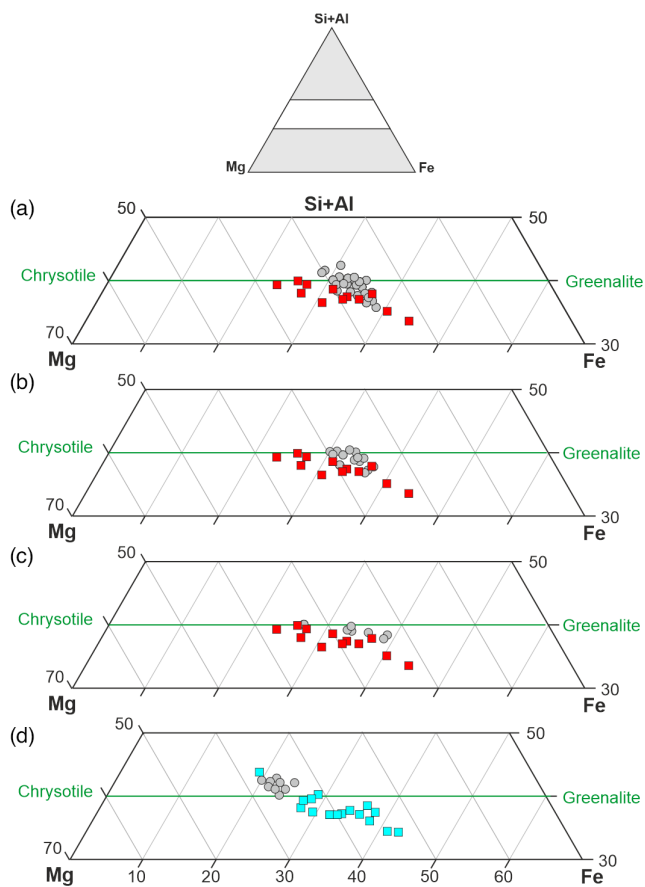


FIGURE 5. Ternary diagrams (atom%) of the chemical composition of various fine-grained rims constituents of LAP 02239 and the xenolith as determined by X-ray microanalysis. Data from LAP 02239 and the xenolith are plotted as gray circles. The red squares in (a–c) are the average compositions of the fine-grained rims of 12 CMs in Zolensky et al. (1993), and the light blue squares in (d) are the average compositions of the matrices of 18 CMs in Zolensky et al. (1993). Green is the solid solution line between Mg- and Fe-serpentine (chrysotile and greenalite, respectively). (a) Fine-grained rims on LAP 02239 chondrules ( $n = 22$  analyses). (b) The xenolith's fine-grained rim ( $n = 16$  analyses). (c) Rims to tochilinite–serpentine grains ( $n = 9$  analyses). (d) The xenolith's fine-grained matrix ( $n = 18$  analyses). The matrix has a lower proportion of iron than all but one of the 18 CMs plotted for comparison (Allan Hills 83016). Data from all of the analyses of LAP 02239 and the xenolith are listed in Table S3. (Color figure can be viewed at [wileyonlinelibrary.com](http://wileyonlinelibrary.com).)

et al., 2007) and “tochilinite–cronstedtite intergrowths” (TCI; Lentfort et al., 2021). The tochilinite–serpentine grains that characterize the light lithology of LAP 02239 are petrographically similar to PCPs and TCIs yet are chemically distinct. Specifically, their ratios of  $\text{FeO}/\text{SiO}_2$  (3.2–5.4, average 4.4) and  $\text{S}/\text{SiO}_2$  (0.7–1.2, average 1.0) (Table S3) are inconsistent with the compositional ranges of PCPs and TCIs that are used in petrologic subtype classifications (Lentfort et al., 2021; Rubin, 2015; Rubin et al., 2007). Specifically, the average  $\text{S}/\text{SiO}_2$  ratio of LAP

02239 tochilinite–serpentine (1.0) is considerably greater than the same ratio of TCIs in the least altered meteorite described by Lentfort et al. (2021) (0.67 for a CM2.9). The average  $\text{FeO}/\text{SiO}_2$  ratio of the LAP 02239 tochilinite–serpentine grains (4.4) is equivalent to a CM2.7 classification of Rubin (2015) and a CM2.8 of Lentfort et al. (2021). However, the petrologic type of LAP 02239 as determined by Alexander et al. (2013) and Howard et al. (2015) is incompatible with the very mild alteration indicated by comparing the tochilinite–serpentine grains with PCP- and TCI-related subtype classifications. We therefore conclude that LAP 02239 was aqueously altered under subtly different conditions to some of the other CMs.

### Accretion and Lithification of the Xenolith's Parent Body

The nature of the xenolith's constituents can help constrain where/when its parent body accreted relative to the parent bodies of known meteorite groups. The xenolith's chondrules are comparable in petrography, mineralogy, and size with those in LAP 02239 and other CMs (Floyd & Lee, 2022b; Hanowski & Brearley, 2001) and are equally as abundant (i.e., 2.4 vs. 2.0 whole chondrules/ $\text{mm}^2$  for the xenolith and LAP 02239, respectively). The oxygen isotope ratios of the xenolith's olivine and pyroxene grains are similar to those of chondrule silicates in other CMs such as Murchison (Figure 8). A CM affinity for the xenolith is also consistent with its pentlandite-rimmed pyrrhotite grain, which is petrographically comparable with primary sulfides in LAP 02239 and the CMs (Singerling & Brearley, 2018, 2020), although in contrast to LAP 02239 the xenolith's pyrrhotite grain lacks magnetite (compare Figures 6c and 7e). As regards CAIs, there are good petrographic and mineralogical similarities between those in the xenolith and in the CMs (Greenwood et al., 1994; MacPherson & Davis, 1994; Rubin, 2007, 2015). However, the average size of the xenolith's CAIs is a third of that of inclusions in LAP 02239, and 23%, 21%, and 14% of the size of those in Paris, QUE 97990, and Mighei, respectively (Table 2). The abundance of CAIs in the xenolith ( $7.28/\text{mm}^2$ ) is also much greater than in the five CMs in Table 2 ( $0.10$ – $0.93/\text{mm}^2$ ) and in the CM2 meteorites, Murray ( $0.90$  and  $0.58/\text{mm}^2$  for two thin sections; Lee & Greenwood, 1994) and Cold Bokkveveld ( $0.6$ – $0.8/\text{mm}^2$  for four thin sections; Greenwood et al., 1994).

As the xenolith contains only a small number of chondrules, CAIs and sulfides, care must be taken not to over-interpret their significance. Nonetheless, the petrographic, mineralogical, and oxygen isotopic parallels between objects in the xenolith, LAP 02239, and other CMs are consistent with the xenolith's parent body having accreted material from a similar part of the protoplanetary disc as the CM parent body(ies) (i.e., the “CM nursery”). It is unlikely that the unusually high abundance of small CAIs in the xenolith is just due to the detailed imaging and

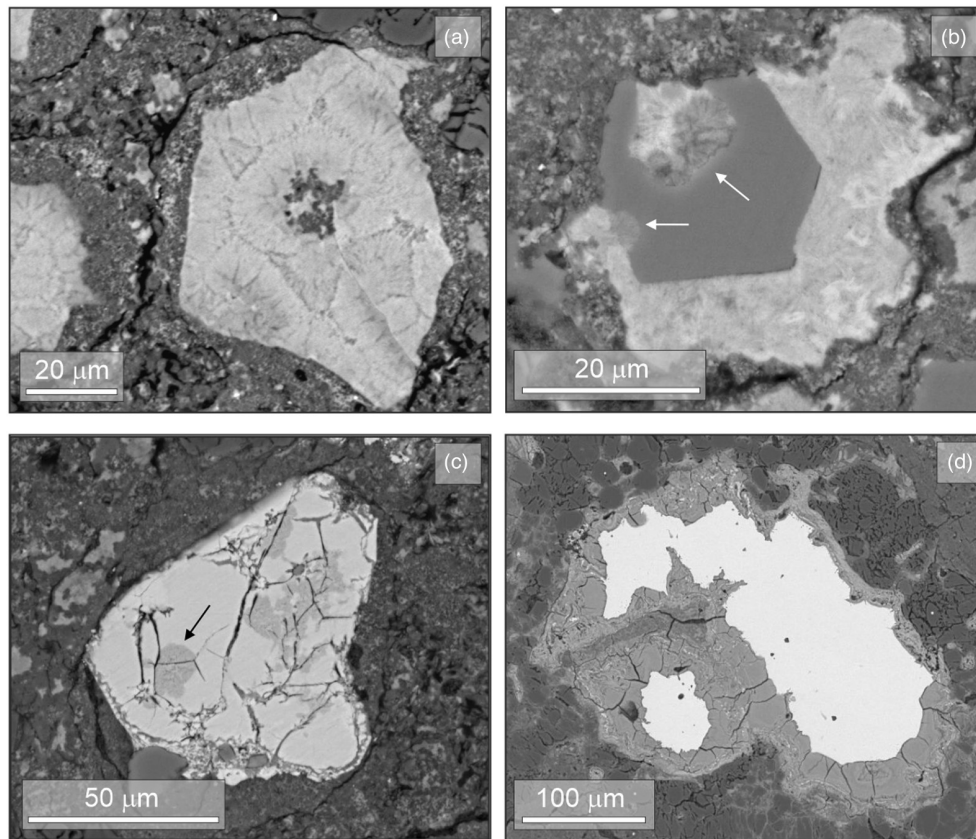


FIGURE 6. Backscattered electron (BSE) images of Fe-rich grains in LAP 02239. (a) A tochilinite–serpentine grain with a narrow rim. Fibers radiate from the grain’s outer edge inwards, and from its core outwards. (b) A Ca-carbonate crystal within a tochilinite–serpentine grain. The crystal is embayed by arrays of tochilinite–serpentine fibers in its upper part and left-hand edge (arrowed). (c) A grain of pyrrhotite with a narrow rim of pentlandite. Parts of the pyrrhotite interior have been altered to Fe-oxide (arrowed). (d) A large grain of Fe,Ni metal (white) within a type I chondrule. The metal has a thick rim of akaganéite (mid-gray).

analytical work undertaken on that relatively small object in comparison with LAP 02239 and other CMs. It is more probable that the xenolith’s parent body preferentially accreted a size-sorted subset of the CAI population. A crucial difference between the xenolith and other CMs including LAP 02239 is that its chondrules and CAIs lack fine-grained rims. The absence of fine-grained rims on the xenolith’s CAIs may be due to their small size (five of the six CAIs are less than 32  $\mu\text{m}$ ) given that 5 of the 10 smallest CAIs in LAP 02239 (i.e., those less than 30  $\mu\text{m}$  in size) also lack rims (Table S2). However, the same explanation cannot apply to chondrules X1 and X2 because all whole chondrules in LAP 02239 that are of a similar size and smaller in size have fine-grained rims (Figure 4a). It is possible that fine-grained rims were once present on X1 and X2 but they were abraded away prior to the chondrules’ accretion into the xenolith’s parent body or have been obscured by aqueous alteration. The former is inconsistent with X1 and X2 being intact (i.e., abrasion would have had to be selective to the rims and not affected the chondrules themselves) and the latter possibility is unlikely given that the xenolith’s fine-grained rim can be readily distinguished

from its matrix (Figure 4c). We are therefore confident that the xenolith’s chondrules never acquired fine-grained rims, and the significance of finding is discussed further below.

The xenolith must have been derived from a lithified part of its parent body for it to have retained its integrity during impact-ejection, passage through the protoplanetary disk, and incorporation into the LAP 02239 parent body. Lithification could have been by compaction and/or aqueous alteration. Given that the xenolith lacks evidence for compaction (e.g., a petrofabric), aqueous alteration is assumed to have been responsible, and its effects are evidenced by the presence of hydrous phases in the mesostasis of its chondrules, its CAIs, and its matrix. The absence of tochilinite–serpentine grains and calcite from the xenolith, and the chemical composition of its matrix (iron-poor relative to the matrices of 17 of the 18 CMs plotted in Figure 5d), shows that the aqueous fluids were depleted in calcium and iron relative to those that altered many other CMs. However, the oxygen isotopic composition of the xenolith’s matrix overlaps with bulk analyses of CM matrices (Clayton & Mayeda, 1999), although it is distinct from the matrices of C1I and all but



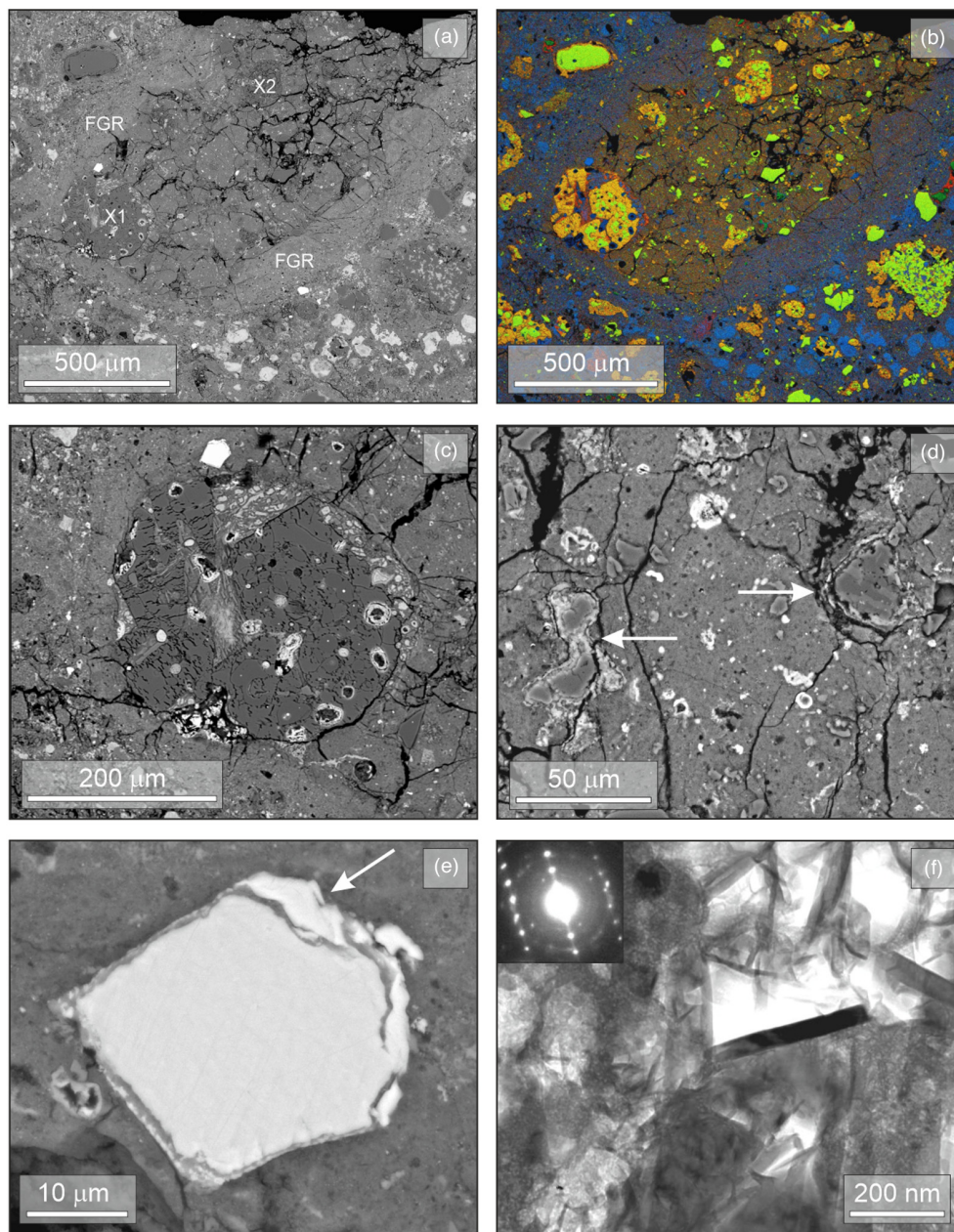


FIGURE 7. (a) Backscattered electron (BSE) image of the xenolith and its fine-grained rim (FGR). The xenolith contains two whole chondrules (X1 and X2), and its matrix is highly fractured. (b) Color blended X-ray map of the xenolith: Fe blue, Mg light green and Si red. These colors render En-rich clinopyroxene orange, Fo-rich olivine light green, high-Z (Fe rich) particles blue, and the xenolith's matrix brown. (c) BSE image of chondrule X1. Its mesostasis has been aqueously altered but grains of Fo-rich olivine and En-rich pyroxene are intact. The chondrule contains rounded voids with a Fe-rich lining, which are probably former blebs of metal. (d) BSE image of two calcium- and aluminum-rich inclusions (CAIs) (arrowed) in the xenolith's matrix. The CAI on the right-hand side has a core of spinel and hibonite, and a rim of diopside. (e) BSE image of a pyrrhotite grain with a rim of pentlandite (arrowed) in the xenolith's matrix. (f) Bright-field TEM image with inset selected area electron diffraction (SAED) pattern of the xenolith's matrix. The SAED pattern is from the lath-shaped crystal in the middle of the field of view, and its main row of spots has a d-spacing of 0.72 nm. (Color figure can be viewed at [wileyonlinelibrary.com](http://wileyonlinelibrary.com).)

one of the C2-ung meteorites analyzed by Rowe et al. (1994; Figure 8). As the oxygen isotopic compositions of CM matrices are determined mainly by the interaction between two reservoirs,  $^{16}\text{O}$ -rich anhydrous silicates and  $^{16}\text{O}$ -poor

water (Clayton & Mayeda, 1999), both components must have been isotopically comparable between the xenolith's parent body and the CMs. Overall, therefore, the xenolith's primary constituents (e.g., chondrules) and secondary phases



TABLE 4. NanoSIMS analyses of the xenolith's chondrules and matrix.

Phase analyzed	Analysis point	$\delta^{18}\text{O}$		$\delta^{17}\text{O}$		$\Delta^{17}\text{O}$	
		$2\sigma$		$2\sigma$		$2\sigma$	
Chondrule X1 olivine	X1 ol-1	-1.4	0.9	-6.0	1.2	-5.3	1.0
Chondrule X1 olivine	X1 ol-2	-2.1	0.9	-6.3	1.2	-5.2	1.0
Chondrule X1 olivine	X1 ol-3	-1.9	0.9	-5.4	1.2	-4.4	1.0
Chondrule X2 olivine	X2 ol-4	0.5	0.9	-3.3	1.2	-3.6	1.0
Chondrule X1 pyroxene	X1 px-1	-3.5	0.9	-7.1	1.2	-5.3	1.0
Chondrule X2 pyroxene	X2 px-1	-0.7	0.9	-4.6	1.2	-4.3	1.0
Matrix	Matrix-1	10.5	0.9	3.2	1.2	-2.3	1.0
Matrix	Matrix-2	11.6	0.9	4.0	1.2	-2.0	1.0
Matrix	Matrix-3	9.4	0.9	2.8	1.2	-2.1	1.0
Matrix	Matrix-4	12.7	0.9	4.3	1.2	-2.4	1.0
Matrix	Matrix-5	12.2	0.9	5.6	1.2	-0.7	1.0
Matrix	Matrix-6	11.8	0.9	4.9	1.2	-1.3	1.0
Matrix	Matrix-7	8.5	0.9	2.8	1.2	-1.6	1.0

Note: Images of the analysis points are in Figures S3 and S4.

(e.g., matrix serpentine) show that its parent body was quite similar in construction and geological evolution to the CM parent body(ies).

### Transfer of the Xenolith and its Incorporation into the LAP 02239 Parent Body

The xenolith's fine-grained rim is comparable in petrography and chemical composition with rims on chondrules and other objects elsewhere in LAP 02239, and in different CM meteorites (e.g., Figure 5). Other groups of CCs and ordinary chondrites also have fine-grained rims on chondrules and other objects, although not in the same abundance as the CMs (e.g., Alexander, 1995; Brearley, 1993; Krot et al., 1998). The fine-grained rims formed by the accretion of dust onto objects that were free floating in the protoplanetary disc (Cuzzi, 2004; Hanna & Ketcham, 2018; Metzler et al., 1992). Alexander et al. (2008) developed a model whereby chondrules form in high-density regions (clumps), in response to a process such as shock heating, then other material (e.g., dust, CAIs) enters the clump as it collapses by self-gravitation. However, the absence of fine-grained rims on the xenolith's chondrules is at odds with that model if they formed contemporaneously with chondrules in the CMs. In addition, the presence of fine-grained rims on LAP 02239 CAIs and the xenolith argues against the dust being present only as a halo around the chondrule-forming region and in favor of it being distributed more widely around the CM nursery; this dust may also

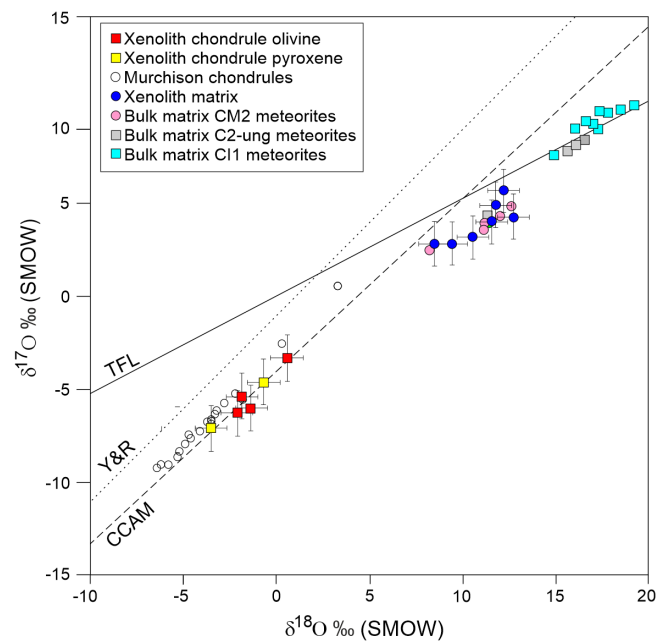


FIGURE 8. Oxygen isotopic composition of the xenolith's matrix, and grains of olivine and pyroxene in its chondrules. Also plotted for comparison are SIMS analyses of type I chondrules in Murchison (Chaumard et al., 2018), and bulk analyses of the matrices of the C2-ung meteorites Bells and Essebi (Rowe et al., 1994), the C11 meteorites Alais, Ivuna, and Orgueil (Rowe et al., 1994), and CM2 meteorites Cold Bokkeveld, Lewis Cliff 85311, Mighei, Murchison, Murray, and Nogoya (Clayton & Mayeda, 1999). TFL = Terrestrial Fractionation Line, Y&R = Young and Russell slope 1 line (Young & Russell, 1998), CCAM = Carbonaceous Chondrite Anhydrous Mineral line (Clayton & Mayeda, 1999; Clayton et al., 1977). (Color figure can be viewed at wileyonlinelibrary.com.)

TABLE 5. History of the LAP 02239 xenolith.

1. Accretion of un-rimmed chondrules and calcium- and aluminum-rich inclusions (CAIs) into the xenolith's parent body
2. Lithification of the xenolith's parent body by aqueous alteration
3. Impact-ejection of the xenolith from its parent body
4. Accretion of a fine-grained rim on the xenolith as it passed through a dust-rich region of the protoplanetary disc
5. Incorporation of the rimmed xenolith into the LAP 02239 parent body along with rimmed chondrules and CAIs
6. Aqueous alteration of the LAP 02239 parent body including the xenolith's fine-grained rim
7. Fracturing of the xenolith's matrix during deformation of the LAP 02239 parent body
8. Ejection of LAP 02239 from its parent body, fall in Antarctica, terrestrial alteration of Fe,Ni metal

have been present at a lower density where the parent bodies of other CC groups were forming. A corollary of this model is that rim-forming dust was absent when and where the

xenolith's chondrules were moving through the protoplanetary disc. Thus, the similarities and differences between the xenolith's chondrules and those in the CMs show that its parent body accreted in a similar region of the protoplanetary disc as the CM nursery, but not when/where rim-forming dust was present.

### Aqueous Alteration and Compaction of the LAP 02239 Parent Body

Given that the xenolith passed through a dust-rich region of the protoplanetary disc contemporaneously with CM chondrules, it is most likely to have been accreted into the LAP 02239 parent body at the same time as them. When the LAP 02239 parent body was aqueously altered, it must therefore have contained the xenolith. Such a timing differs from previously studied xenoliths, which are interpreted to have been incorporated after aqueous alteration of their host CM (Lindgren et al., 2013; Olsen et al., 1988; Zhang et al., 2010). Nonetheless, incorporation of the xenolith into the LAP 02239 parent body at such an early stage is consistent with the nature of its fine-grained rim, which is petrographically and chemically comparable with the rims on LAP 02239 chondrules and other objects indicating aqueous alteration from fluids of a similar composition.

There is no evidence for whether the xenolith was affected by aqueous alteration of the LAP 02239 parent body. However, the absence of carbonates and tochilinite suggests that any overprinting was minimal, which was probably because the xenolith was enclosed by a fine-grained rim and most of the phases that would have been susceptible to aqueous fluids had already been altered on the xenolith's parent body. The sharpness of the contact between the xenolith's matrix and its fine-grained rim is also consistent with limited overprinting (Figure 4c). The intense fracturing of the xenolith's matrix is interpreted to have taken place after the xenolith had acquired its fine-grained rim because the rim is cut by some of the fractures. In addition, the xenolith would have disintegrated upon fracturing if it had not been enclosed by a fine-grained rim. The cause of the fracturing is inferred to have been lithostatic or dynamic compaction of the parent body, although such deformation must have been mild because the host meteorite has only a weak chondrule-defined petrofabric. The brittleness of the xenolith's matrix relative to its fine-grained rim probably reflects the distinctive nature of the xenolith's aqueous alteration products (e.g., very finely crystalline serpentine).

The last process recorded by LAP 02239 is the partial alteration of large Fe,Ni metal grains to akaganéite, which is a common product of Antarctic weathering (Buchwald & Clarke, 1995; Lee & Bland, 2004). It is also during this phase of water/rock interaction that the rounded voids in xenolith chondrule X1 are interpreted to have formed, by dissolution of Fe,Ni metal or sulfide.

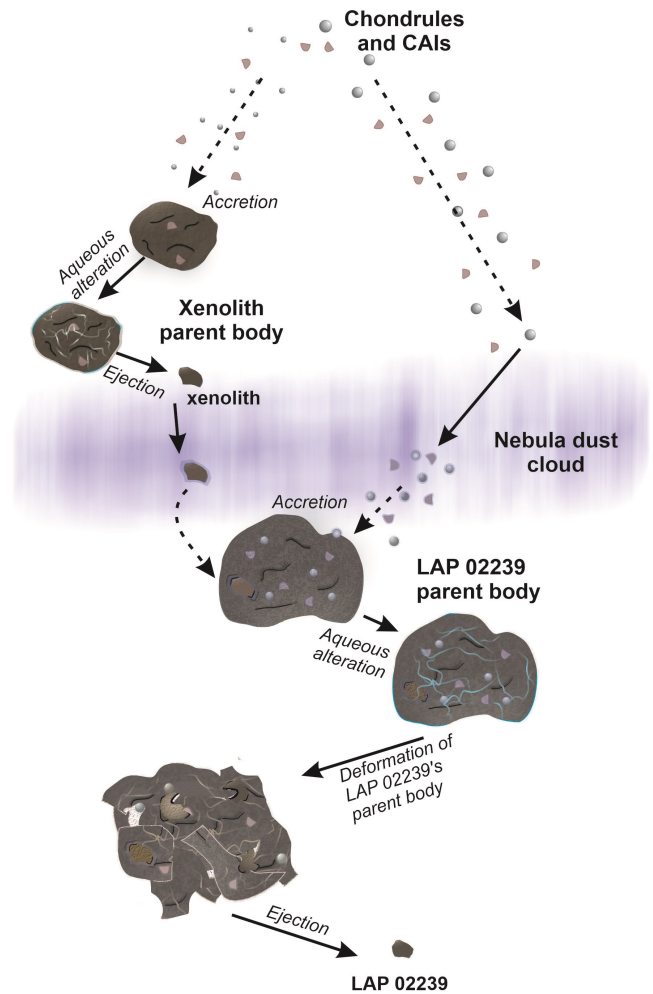


FIGURE 9. Cartoon diagram summarizing the history of the xenolith and its parent bodies. (Color figure can be viewed at [wileyonlinelibrary.com](http://wileyonlinelibrary.com).)

These effects are consistent with the weathering grade B classification for LAP 02239. The xenolith's history is summarized in Table 5 and Figure 9.

### Implications for Understanding Early Solar System History

#### *The Origins of Cognate Clasts and Xenoliths in the CMs*

LAP 02239 contains the only xenolith with a fine-grained rim that has been described from a CM, although others are likely to occur. For example, using X-ray computed tomography, Hanna and Ketcham (2018) described a rimmed object in Murchison that could be a lithic clast or xenolith.

As all of the xenoliths that have been previously described from the CMs are un-rimmed, they are interpreted to have moved through the protoplanetary disc after rim-forming dust had dissipated or been consumed. Such a late-stage timing is consistent with those xenoliths having been

incorporated into a CM parent body after it had been aqueously altered. Thus, rim-forming dust was present in the vicinity of the CM nursery before and probably during parent body accretion; the presence of fine-grained rims on chondrules in other CC groups (Brearley, 1993; Krot et al., 1998) shows that dust was distributed widely throughout the protoplanetary disc. The absence of fine-grained rims from cognate clasts (Figure 1a) could also be due to their late-stage transport and incorporation. However, as many of them are likely to be pieces of the same parent body that have just been redistributed, they would not have traveled sufficiently far through the protoplanetary disc to have interacted with rim-forming dust even if it was still present. Such locally derived clasts have been described from the Aguas Zarcas (CM2) meteorite by Yang et al. (2022), and they suggest that the ejection and re-accretion of such millimeter- to centimeter-size “pebbles” has been observed on the asteroid Bennu by the OSIRIS-REx spacecraft.

### Chronology of CC Aqueous Alteration

Owing to the lack of dateable secondary minerals in the xenolith (e.g., carbonates), it is not possible to determine when it was aqueously altered. The  $^{53}\text{Mn}$ - $^{53}\text{Cr}$  ages of carbonates in various groups of CCs (CI, CR, CM, C2-ung) cluster at  $\sim 4 \pm 2$  Ma after CAI formation at  $\sim 4567.2$  Ma, which has been interpreted to reflect the time scales of accretion of parent bodies and their heating by  $^{26}\text{Al}$  decay (Bischoff et al., 2021; Fujiya et al., 2012; Lee et al., 2012; Visser et al., 2020). If it is assumed that aqueous alteration of the parent bodies of the xenolith and LAP 02239 was also driven by radiogenic decay, then  $^{53}\text{Mn}$ - $^{53}\text{Cr}$  ages constrain the time scale of the processes listed in Table 5 and depicted in Figure 9. Specifically, the xenolith was aqueously altered in one parent body that had been heated by  $^{26}\text{Al}$ , transferred through the protoplanetary disc, then accreted into another parent body that had incorporated sufficient  $^{26}\text{Al}$  to drive aqueous alteration.

### CONCLUSIONS

Rimmed xenoliths in CM chondrites can provide unique insights into some of the protoplanetary disc's earliest formed bodies. The nature of the chondrules and CAIs in the LAP 02239 xenolith, and the oxygen isotopic composition of its matrix, indicates that its parent body accreted in a similar region of the protoplanetary disc as the CM nursery. However, that body accreted at a very early stage such that it had been aqueously altered significantly before construction of the LAP 02239 parent body. Thus, the LAP 02239 xenolith shows that CC parent bodies did not accrete and geologically evolve in lockstep, but rather formed and geologically evolved over a period of time albeit within the window of  $^{26}\text{Al}$  heating.

**Acknowledgments**—We thank Billy Smith and Colin How for assistance with the FIB and TEM work. IAF and XZ are grateful for STFC funding through grant ST/T000228/1 for NanoSIMS measurements, and MRL thanks the STFC for support through grants ST/T002328/1 and ST/W001128/1. We thank the Natural History Museum, London, for the loan of Cold Bokkeveld BM1727, and to ANSMET for the loan of LAP 02239. US Antarctic meteorite samples are recovered by the Antarctic Search for Meteorites (ANSMET) program, which has been funded by NSF and NASA, and characterized and curated by the Department of Mineral Sciences of the Smithsonian Institution and Astromaterials Acquisition and Curation Office at NASA Johnson Space Center. We are very grateful to Conel Alexander and Samuel Ebert for their knowledgeable and constructive reviews, and an associate editor Josep Trigo-Rodríguez.

**Data Availability Statement**—The data that support the findings of this study are available in the supplementary material of this article.

**Editorial Handling**—Dr. Josep M. Trigo-Rodríguez

### REFERENCES

- Alexander, C. M. O'D. 1995. Trace Element Contents of Chondrule Rims and Interchondrule Matrix in Ordinary Chondrites. *Geochimica et Cosmochimica Acta* 59: 3247–66.
- Alexander, C. M. O'D., Grossman, J. N., Ebel, D. S., and Ciesla, F. J. 2008. The Formation Conditions of Chondrules and Chondrites. *Science* 320: 1617–9.
- Alexander, C. M. O'D., Howard, K. T., Bowden, R., and Fogel, M. L. 2013. The Classification of CM and CR Chondrites Using Bulk H, C and N Abundances and Isotopic Compositions. *Geochimica et Cosmochimica Acta* 123: 244–60.
- Barber, D. J. 1981. Matrix Phyllosilicates and Associated Minerals in C2M Carbonaceous Chondrites. *Geochimica et Cosmochimica Acta* 45: 945–70.
- Bischoff, A., Alexander, C. M. O'D., Barrat, J. A., Burkhardt, C., Busemann, H., Degering, D., di Rocco, T., et al. 2021. The Old, Unique C1 Chondrite Flensburg—Insight into the First Processes of Aqueous Alteration, Brecciation, and the Diversity of Water-Bearing Parent Bodies and Lithologies. *Geochimica et Cosmochimica Acta* 293: 142–86.
- Bischoff, A., Scott, E. R. D., Metzler, K., and Goodrich, C. A. 2006. Nature and Origins of Meteoritic Breccias. In *Meteorites and the Early Solar System II*, edited by D. S. Lauretta, and H. Y. McSween, Jr., 679–712. Tucson: University of Arizona Press.
- Brearley, A. J. 1993. Matrix and Fine-Grained Rims in the Unequilibrated CO3 Chondrite, ALHA77307: Origins and Evidence for Diverse, Primitive Nebular Dust Components. *Geochimica et Cosmochimica Acta* 57: 1521–50.
- Buchwald, V. F., and Clarke, R. S. 1995. Corrosion of Fe-Ni Alloys by Cl-Containing akaganéite ( $\beta$ -FeOOH): The Antarctic Meteorite Case. *American Mineralogist* 74: 656–67.
- Bunch, T. E., and Chang, S. 1980. Carbonaceous Chondrites—II. Carbonaceous Chondrite Phyllosilicates and Light



- Element Geochemistry as Indicators of Parent Body Processes and Surface Conditions. *Geochimica et Cosmochimica Acta* 44: 1543–77.
- Burbine, T. 2016. *Asteroids: Astronomical and Geological Bodies (Cambridge Planetary Science)*. Cambridge: Cambridge University Press.
- Chaumard, N., Defouilloy, C., and Kita, N. T. 2018. Oxygen Isotope Systematics of Chondrules in the Murchison CM2 chondrite and Implications for the CO-CM Relationship. *Geochimica et Cosmochimica Acta* 228: 220–42.
- Clayton, R. N., and Mayeda, T. K. 1999. Oxygen Isotope Studies of Carbonaceous Chondrites. *Geochimica et Cosmochimica Acta* 63: 2089–104.
- Clayton, R. N., Onuma, N., Grossman, L., and Mayeda, T. K. 1977. Distribution of Pre-Solar Component in Allende and Other Carbonaceous Chondrites. *Earth and Planetary Science Letters* 34: 209–24.
- Cuzzi, J. N. 2004. Blowing in the Wind: III. Accretion of Dust Rims by Chondrule-Sized Particles in a Turbulent Protoplanetary Nebula. *Icarus* 168: 484–97.
- Ebert, S., Bischoff, A., Harries, D., Lentfort, S., Barrat, J.-A., Pack, A., Gattacceca, J., Visser, R., Schmid-Beurmann, P., and Kimpe, I. S. 2019. Northwest Africa 11024—A Heated and Dehydrated Unique Carbonaceous (CM) Chondrite. *Meteoritics & Planetary Science* 54: 328–56.
- Ebert, S., Patzek, M., Lentfort, S., and Bischoff, A. 2019. Accretion of Differentiated Achondritic and Aqueously Altered Chondritic Materials in the Early Solar System—Significance of an Igneous Fragment in the CM Chondrite NWA 12651. *Meteoritics & Planetary Science* 54: 2985–95.
- Floyd, C. J., and Lee, M. R. 2022a. The CIS Method: A Proposed Standardised Protocol for Measuring and Reporting Sizes of Chondrules and Other Chondritic Objects. 85th Annual Meeting of the Meteoritical Society, abstract #6087.
- Floyd, C. J., and Lee, M. R. 2022b. A New Record of Chondrule Sizes within Carbonaceous CM Chondrites and Implications for Understanding the CM-CO Chondrite Clan. 85th Annual Meeting of the Meteoritical Society, abstract #2695.
- Fuchs, L. H., Olsen, E., and Jensen, K. J. 1973. Mineralogy, Mineral-Chemistry, and Composition of the Murchison (C2) Meteorite. *Smithsonian Contributions to the Earth Sciences* 10: 39.
- Fujiya, W., Sugiura, N., Hotta, H., Ichimura, K., and Sano, Y. 2012. Evidence for the Late Formation of Hydrous Asteroids from Young Meteoritic Carbonates. *Nature Communications* 3: 627.
- Greenwood, R. C., Lee, M. R., Hutchison, R., and Barber, D. J. 1994. Formation and Alteration of CAIs in Cold Bokkeveld (CM2). *Geochimica et Cosmochimica Acta* 58: 1913–35.
- Hanna, R. D., and Ketcham, R. A. 2018. Evidence for Accretion of Fine-Grained Rims in a Turbulent Nebula for CM Murchison. *Earth and Planetary Science Letters* 481: 201–11.
- Hanowski, N. P., and Brearley, A. J. 2001. Aqueous Alteration of Chondrules in the CM Carbonaceous Chondrite, Allan Hills 81002: Implications for Parent Body Alteration. *Geochimica et Cosmochimica Acta* 65: 495–518.
- Hoppe, P., Cohen, S., and Meibom, A. 2013. NanoSIMS: Technical Aspects and Applications in Cosmochemistry and Biological Geochemistry. *Geostandards and Geoanalytical Research* 37: 111–54.
- Howard, K. T., Alexander, C. M. O'D., Schrader, D. L., and Dyl, K. A. 2015. Classification of Hydrous Meteorites (CR, CM and C2 Ungrouped) by Phyllosilicate Fraction: PSD-XRD Modal Mineralogy and Planetsimal Environments. *Geochimica et Cosmochimica Acta* 149: 206–22.
- Howard, K. T., Benedix, G. K., Bland, P. A., and Cressey, G. 2009. Modal Mineralogy of CM2 Chondrites by X-Ray Diffraction (PSD-XRD). Part 1: Total Phyllosilicate Abundance and the Degree of Aqueous Alteration. *Geochimica et Cosmochimica Acta* 73: 4576–89.
- Howard, K. T., Benedix, G. K., Bland, P. A., and Cressey, G. 2011. Modal Mineralogy of CM Chondrites by X-Ray Diffraction (PSD-XRD). Part 2: Degree, Nature and Settings of Aqueous Alteration. *Geochimica et Cosmochimica Acta* 75: 2735–51.
- Kerrouach, I., Bischoff, A., Zolensky, M. E., Pack, A., Patzek, M., Hanna, R. D., Fries, M. D., et al. 2021. The Polymict Carbonaceous Breccia Aguas Zarcas: A Potential Analog to Samples Being Returned by the OSIRIS-REX and Hayabusa2 Missions. *Meteoritics & Planetary Science* 56: 277–310.
- Kerrouach, I., Ebert, S., Patzek, M., Bischoff, A., Zolensky, M. E., Pack, A., Schmitt-Koppline, P., Belhai, D., Bendaoud, A., and Le, L. 2019. A Light, Chondritic Xenolith in the Murchison (CM) Chondrite—Formation by Fluid-Assisted Percolation during Metasomatism? *Geochemistry* 79: 125518.
- Krot, A. N., Petaev, M. I., Scott, E. R. D., Choi, B.-G., Zolensky, M. E., and Keil, K. 1998. Progressive Alteration in CV3 Chondrites: More Evidence for Asteroidal Alteration. *Meteoritics & Planetary Science* 33: 1065–85.
- Lee, M. R., and Bland, P. A. 2004. Mechanisms of Weathering of Meteorites Recovered from Hot and Cold Deserts and the Formation of Phyllosilicates. *Geochimica et Cosmochimica Acta* 68: 893–916.
- Lee, M. R., Bland, P. A., and Graham, G. 2003. Preparation of TEM Samples by Focused Ion Beam (FIB) Techniques: Applications to the Study of Clays and Phyllosilicates in Meteorites. *Mineralogical Magazine* 67: 581–92.
- Lee, M. R., Daly, L., Floyd, C., and Martin, P.-E. 2021. CM Carbonaceous Chondrite Falls and their Terrestrial Alteration. *Meteoritics & Planetary Science* 56: 34–48.
- Lee, M. R., and Greenwood, R. C. 1994. Alteration of calcium- and aluminium-rich inclusions (CAIs) in the Murray (CM2) carbonaceous chondrite. *Meteoritics* 29: 780–90.
- Lee, M. R., Lindgren, P., and Sofe, M. R. 2014. Aragonite, Breunnerite, Calcite and Dolomite in the CM Carbonaceous Chondrites: High Fidelity Recorders of Progressive Parent Body Aqueous Alteration. *Geochimica et Cosmochimica Acta* 144: 126–56.
- Lee, M. R., Lindgren, P., Sofe, M. R., Alexander, C. M. O'D., and Wang, J. 2012. Extended Chronologies of Aqueous Alteration in the CM2 Carbonaceous Chondrites: Evidence from Queen Alexandra Range 93005. *Geochimica et Cosmochimica Acta* 92: 148–69.
- Lentfort, S., Bischoff, A., Ebert, S., and Patzek, M. 2021. Classification of CM Chondrite Breccias—Implications for the Evaluation of Samples from the OSIRIS-REX and Hayabusa2 Missions. *Meteoritics & Planetary Science* 56: 127–47.
- Lindgren, P., Lee, M. R., Sofe, M. R., and Zolensky, M. E. 2013. Clasts in the CM2 Carbonaceous Chondrite Lonewolf Nunataks 94101: Evidence for Aqueous Alteration Prior to Complex Mixing. *Meteoritics & Planetary Science* 48: 1074–90.
- MacPherson, G. J., and Davis, A. M. 1994. Refractory Inclusions in the Prototypical CM Chondrite, Mighei. *Geochimica et Cosmochimica Acta* 58: 5599–625.

- McSween, H. Y., Jr. 1979a. Are Carbonaceous Chondrites Primitive or Processed? A Review. *Reviews of Geophysics and Space Physics* 17: 1059–78.
- McSween, H. Y., Jr. 1979b. Alteration in CM Carbonaceous Chondrites Inferred from Modal and Chemical Variations in Matrix. *Geochimica et Cosmochimica Acta* 43: 1761–70.
- McSween, H. Y., Jr., and Richardson, S. M. 1977. The Composition of Carbonaceous Chondrite Matrix. *Geochimica et Cosmochimica Acta* 51: 2469–77.
- Metzler, K., Bischoff, A., and Stoffler, D. 1992. Accretionary Dust Mantles in CM Chondrites: Evidence for Solar Nebula Processes. *Geochimica et Cosmochimica Acta* 56: 2873–97.
- Muller, G. 1966. Significance of Inclusions in Carbonaceous Meteorites. *Nature* 210: 151–5.
- Nittler, L. R., Stoud, R. M., Trigo-Rodríguez, J. M., De Gregorio, B. T., Alexander, C. M. O'D., Davidson, J., Moyano-Camero, C. E., and Tanbakouei, S. 2019. A Cometary Building Block in a Primitive Asteroidal Meteorite. *Nature Astronomy* 3: 659–66.
- Olsen, E. J., Davis, A. M., Hutcheon, I. D., Clayton, R. N., Mayeda, T. K., and Grossman, L. 1988. Murchison Xenoliths. *Geochimica et Cosmochimica Acta* 52: 1615–26.
- Rowe, M. W., Clayton, R. N., and Mayeda, T. K. 1994. Oxygen Isotopes in Separated Components of CI and CM Chondrites. *Geochimica et Cosmochimica Acta* 58: 5341–7.
- Rubin, A. E. 2007. Petrography of Refractory Inclusions in CM2.6 QUE 97990 and the Origin of Melilite-Free Spinel Inclusions in CM Chondrites. *Meteoritics & Planetary Science* 42: 1711–26.
- Rubin, A. E. 2015. An American on Paris: Extent of Aqueous Alteration of a CM Chondrite and the Petrography of its Refractory and Amoeboid Olivine Inclusions. *Meteoritics & Planetary Science* 50: 1595–612.
- Rubin, A. E., Trigo-Rodríguez, J. M., Huber, H., and Wasson, J. T. 2007. Progressive Aqueous Alteration of CM Carbonaceous Chondrites. *Geochimica et Cosmochimica Acta* 71: 2361–82.
- Russell, S. S., Folco, L., Grady, M. M., Zolensky, M. E., Jones, R., Richter, K., Zipfel, J., and Grossman, J. N. 2004. The Meteoritical Bulletin, No. 88, 2004 July. *Meteoritics & Planetary Science* 39: A215–72.
- Russell, S. S., Suttle, M. D., and King, A. J. 2022. Abundance and Importance of Petrological Type 1 Chondritic Material. *Meteoritics & Planetary Science* 57: 277–301.
- Scicchitano, M. R., Rubatto, D., Hermann, J., Shen, T., Padrón-Navarta, J. A., Williams, I. S., and Zheng, Y.-F. 2018. In Situ Oxygen Isotope Determination in Serpentine Minerals by Ion Microprobe: Reference Materials and Applications to Ultrahigh-Pressure Serpentinites. *Geostandards and Geoanalytical Research* 42: 459–79.
- Singerling, S. A., and Brearley, A. J. 2018. Primary Iron Sulfides in CM and CR Carbonaceous Chondrites: Insights into Nebular Processes. *Meteoritics & Planetary Science* 53: 2078–106.
- Singerling, S. A., and Brearley, A. J. 2020. Altered Primary Iron Sulfides in CM2 and CR2 Carbonaceous Chondrites: Insights into Parent Body Processes. *Meteoritics & Planetary Science* 55: 496–523.
- Tomeoka, K., and Buseck, P. R. 1985. Indicators of Aqueous Alteration in CM Carbonaceous Chondrites: Microtextures of a Layered Mineral Containing Fe, S, O, and Ni. *Geochimica et Cosmochimica Acta* 49: 2149–63.
- Trigo-Rodríguez, J. M., Rimola, A., Tanbakouei, S., Cabedo-Soto, V., and Lee, M. R. 2019. Accretion of Water in Carbonaceous Chondrites: Current Evidence and Implications for the Delivery of Water to Early Earth. *Space Science Reviews* 215: 18.
- Trigo-Rodríguez, J. M., Rubin, A. E., and Wasson, J. T. 2006. Non-Nebular Origin of Dark Mantles Around Chondrules and Inclusions in CM Chondrites. *Geochimica et Cosmochimica Acta* 70: 1271–90.
- Visser, R., John, T., Whitehouse, M. J., Patzek, M., and Bischoff, A. 2020. A Short-Lived  $^{26}\text{Al}$  Induced Hydrothermal Alteration Event in the Outer Solar System: Constraints from Mn/Cr Ages of Carbonates. *Earth and Planetary Science Letters* 547: 116440.
- Yang, X., Hanna, R. D., Davis, A. M., Neander, A. I., and Heck, P. R. 2022. A Record of Post-Accretion Asteroid Surface Mixing Preserved in the Aguas Zarcas Meteorite. *Nature Astronomy* 6: 1051–8.
- Young, E. D., and Russell, S. S. 1998. Oxygen Reservoirs in the Early Solar Nebula Inferred from an Allende CAI. *Science* 282: 2377–88.
- Zhang, A., Guan, Y., Hsu, W., Liu, Y., and Taylor, L. A. 2010. Origin of a Metamorphosed Lithic Clast in CM Chondrite Grove Mountains 021536. *Meteoritics & Planetary Science* 45: 238–2106.
- Zolensky, M. E., Barrett, R., and Browning, L. 1993. Mineralogy and Composition of Matrix and Chondrule Rims in Carbonaceous Chondrites. *Geochimica et Cosmochimica Acta* 57: 3123–48.
- Zolensky, M. E., Mittlefehldt, D. W., Lipschutz, M. E., Wang, M.-S., Clayton, R. N., Mayeda, T. K., Grady, M. N., Pillinger, C., and Barber, D. 1997. CM Chondrites Exhibit the Complete Petrologic Range from Type 2 to 1. *Geochimica et Cosmochimica Acta* 61: 5099–115.

## SUPPORTING INFORMATION

Additional supporting information may be found in the online version of this article.

**Figure S1.** BSE image of the whole polished block of LAP 02239 and a rose diagram showing the orientations of the long axes of its 150 whole chondrules.

**Figure S2.** Ternary diagram of the chemical compositions (atom%) of tochilinite–serpentine grains as determined by X-ray microanalysis ( $n = 24$  analyses).

**Figure S3.** BSE images of xenolith chondrules X1 and X2 showing the location of nanoSIMS analysis points.

**Figure S4.** BSE images of xenolith's matrix showing the location of nanoSIMS analysis points.

**Table S1.** Size of chondrules in LAP 02239 and the xenolith.

**Table S2.** Size and mineralogy of CAIs in LAP 02239 and the xenolith.

**Table S3.** Chemical analyses of constituents of LAP 02239 and the xenolith.